



# Real-time visualization of two-photon fluorescence lifetime imaging microscopy using a wavelength-tunable femtosecond pulsed laser

JIHEUN RYU,<sup>1,2</sup> UNGYO KANG,<sup>3</sup> JAYUL KIM,<sup>1</sup> HYUNJUN KIM,<sup>1</sup> JUE HYUNG KANG,<sup>3</sup> HYUNJIN KIM,<sup>4</sup> DAE KYUNG SOHN,<sup>5</sup> JAE-HEON JEONG,<sup>1</sup> HONGKI YOO,<sup>3,6</sup> AND BOMI GWEON<sup>3,7</sup>

<sup>1</sup>Department of Mechanical Engineering, Korea Advanced Institute of Science and Technology, Daejeon 34141, South Korea

<sup>2</sup>Wellman Center for Photomedicine, Harvard Medical School & Massachusetts General Hospital, Boston, Massachusetts 02114, USA

<sup>3</sup>Department of Biomedical Engineering, Hanyang University, Seoul 04763, South Korea

<sup>4</sup>Molecular Imaging & Therapy Branch, Research Institute and Hospital, National Cancer Center, Goyang, 10408, South Korea

<sup>5</sup>Innovative Medical Engineering & Technology, Division of Convergence Technology, Research Institute and Hospital, National Cancer Center, Goyang, 10408, South Korea

<sup>6</sup>hyoo@hanyang.ac.kr

<sup>7</sup>gweonbomi@gmail.com

**Abstract:** A fluorescence lifetime imaging microscopy (FLIM) integrated with two-photon excitation technique was developed. A wavelength-tunable femtosecond pulsed laser with nominal pulse repetition rate of 76-MHz was used to acquire FLIM images with a high pixel rate of 3.91 MHz by processing the pulsed two-photon fluorescence signal. Analog mean-delay (AMD) method was adopted to accelerate the lifetime measurement process and to visualize lifetime map in real-time. As a result, rapid tomographic visualization of both structural and chemical properties of the tissues was possible with longer depth penetration and lower photo-damage compared to the conventional single-photon FLIM techniques.

© 2018 Optical Society of America under the terms of the [OSA Open Access Publishing Agreement](#)

**OCIS codes:** (110.6880) Three-dimensional image acquisition; (180.2520) Fluorescence microscopy; (180.4315) Nonlinear microscopy; (170.3650) Lifetime-based sensing

## References and links

1. N. Barkai and S. Leibler, "Robustness in simple biochemical networks," *Nature* **387**(6636), 913–917 (1997).
2. M. Y. Berezin and S. Achilefu, "Fluorescence Lifetime Measurements and Biological Imaging," *Chem. Rev.* **110**(5), 2641–2684 (2010).
3. W. Becker, "Fluorescence lifetime imaging--techniques and applications," *J. Microsc.* **247**(2), 119–136 (2012).
4. N. P. Galletly, J. McGinty, C. Dunsby, F. Teixeira, J. Requejo-Isidro, I. Munro, D. S. Elson, M. A. Neil, A. C. Chu, P. M. French, and G. W. Stamp, "Fluorescence lifetime imaging distinguishes basal cell carcinoma from surrounding uninvolved skin," *Br. J. Dermatol.* **159**(1), 152–161 (2008).
5. M. S. Islam, M. Honma, T. Nakabayashi, M. Kinjo, and N. Ohta, "pH Dependence of the Fluorescence Lifetime of FAD in Solution and in Cells," *Int. J. Mol. Sci.* **14**(1), 1952–1963 (2013).
6. J. M. Jabbour, S. Cheng, B. H. Malik, R. Cuenca, J. A. Jo, J. Wright, Y. S. L. Cheng, and K. C. Maitland, "Fluorescence lifetime imaging and reflectance confocal microscopy for multiscale imaging of oral precancer," *J. Biomed. Opt.* **18**(4), 046012 (2013).
7. J. Park, P. Pande, S. Shrestha, F. Clubb, B. E. Applegate, and J. A. Jo, "Biochemical characterization of atherosclerotic plaques by endogenous multispectral fluorescence lifetime imaging microscopy," *Atherosclerosis* **220**(2), 394–401 (2012).
8. P. I. H. Bastiaens and A. Squire, "Fluorescence lifetime imaging microscopy: spatial resolution of biochemical processes in the cell," *Trends Cell Biol.* **9**(2), 48–52 (1999).
9. D. Bray, "Protein Molecules as Computational Elements in Living Cells," *Nature* **376**(6538), 307–312 (1995).
10. S. Cheng, J. J. Rico-Jimenez, J. Jabbour, B. Malik, K. C. Maitland, J. Wright, Y. S. L. Cheng, and J. A. Jo, "Flexible endoscope for continuous in vivo multispectral fluorescence lifetime imaging," *Opt. Lett.* **38**(9), 1515–1517 (2013).

11. T. Hinsdale, C. Olsovsky, J. J. Rico-Jimenez, K. C. Maitland, J. A. Jo, and B. H. Malik, "Optically sectioned wide-field fluorescence lifetime imaging microscopy enabled by structured illumination," *Biomed. Opt. Express* **8**(3), 1455–1465 (2017).
12. J. L. Rinnenthal, C. Börnchen, H. Radbruch, V. Andresen, A. Mossakowski, V. Siffrin, T. Seelemann, H. Spiecker, I. Moll, J. Herz, A. E. Hauser, F. Zipp, M. J. Behne, and R. Niesner, "Parallelized TCSPC for Dynamic Intravital Fluorescence Lifetime Imaging: Quantifying Neuronal Dysfunction in Neuroinflammation," *PLoS One* **8**(4), e60100 (2013).
13. W. Becker, *Advanced Time-Correlated Single Photon Counting Applications* (Springer International Publishing, 2015).
14. S. Cheng, R. M. Cuenca, B. Liu, B. H. Malik, J. M. Jabbour, K. C. Maitland, J. Wright, Y. S. L. Cheng, and J. A. Jo, "Handheld multispectral fluorescence lifetime imaging system for in vivo applications," *Biomed. Opt. Express* **5**(3), 921–931 (2014).
15. B. H. Malik, J. Lee, S. Cheng, R. Cuenca, J. M. Jabbour, Y. S. L. Cheng, J. M. Wright, B. Ahmed, K. C. Maitland, and J. A. Jo, "Objective Detection of Oral Carcinoma with Multispectral Fluorescence Lifetime Imaging In Vivo," *Photochem. Photobiol.* **92**(5), 694–701 (2016).
16. X. Y. Dow, S. Z. Sullivan, R. D. Muir, and G. J. Simpson, "Video-rate two-photon excited fluorescence lifetime imaging system with interleaved digitization," *Opt. Lett.* **40**(14), 3296–3299 (2015).
17. M. G. Giacomelli, Y. Sheikine, H. Vardeh, J. L. Connolly, and J. G. Fujimoto, "Rapid imaging of surgical breast excisions using direct temporal sampling two photon fluorescent lifetime imaging," *Biomed. Opt. Express* **6**(11), 4317–4325 (2015).
18. S. Moon, Y. Won, and D. Y. Kim, "Analog mean-delay method for high-speed fluorescence lifetime measurement," *Opt. Express* **17**(4), 2834–2849 (2009).
19. Y. J. Won, S. Moon, W. T. Han, and D. Y. Kim, "Referencing techniques for the analog mean-delay method in fluorescence lifetime imaging," *J. Opt. Soc. Am. A* **27**(11), 2402–2410 (2010).
20. Y. J. Won, W. T. Han, and D. Y. Kim, "Precision and accuracy of the analog mean-delay method for high-speed fluorescence lifetime measurement," *J. Opt. Soc. Am. A* **28**(10), 2026–2032 (2011).
21. Y. Won, S. Moon, W. Yang, D. Kim, W. T. Han, and D. Y. Kim, "High-speed confocal fluorescence lifetime imaging microscopy (FLIM) with the analog mean delay (AMD) method," *Opt. Express* **19**(4), 3396–3405 (2011).
22. B. Kim, B. Park, S. Lee, and Y. Won, "GPU accelerated real-time confocal fluorescence lifetime imaging microscopy (FLIM) based on the analog mean-delay (AMD) method," *Biomed. Opt. Express* **7**(12), 5055–5065 (2016).
23. J. Kim, J. Ryu, and D. Gweon, "Real-time Fluorescence Lifetime Imaging Microscopy Implementation by Analog Mean-Delay Method through Parallel Data Processing," *Applied Microscopy* **46**(1), 6–13 (2016).
24. J. Ryu, J. Kim, H. Kim, J. H. Jeong, H. J. Lee, H. Yoo, and D. G. Gweon, "High-speed time-resolved laser-scanning microscopy using the line-to-pixel referencing method," *Appl. Opt.* **55**(32), 9033–9041 (2016).
25. H. S. Nam, W. J. Kang, M. W. Lee, J. W. Song, J. W. Kim, W. Y. Oh, and H. Yoo, "Multispectral analog-mean-delay fluorescence lifetime imaging combined with optical coherence tomography," *Biomed. Opt. Express* **9**(4), 1930–1947 (2018).
26. Y. Dancik, A. Favre, C. J. Loy, A. V. Zvyagin, and M. S. Roberts, "Use of multiphoton tomography and fluorescence lifetime imaging to investigate skin pigmentation in vivo," *J. Biomed. Opt.* **18**(2), 026022 (2013).
27. Laser Institute of America, "National Standard for Safe Use of Lasers ANSI Z136.1-2000," (American National Standards Institute, Inc., 2000).
28. P. Kapusta, R. Erdmann, U. Ortmann, and M. Wahl, "Time-resolved fluorescence anisotropy measurements made simple," *J. Fluoresc.* **13**(2), 179–183 (2003).
29. A. S. Kristoffersen, S. R. Erga, B. Hamre, and Ø. Frette, "Testing Fluorescence Lifetime Standards using Two-Photon Excitation and Time-Domain Instrumentation: Rhodamine B, Coumarin 6 and Lucifer Yellow," *J. Fluoresc.* **24**(4), 1015–1024 (2014).
30. C. Li, C. Pitsillides, J. M. Runnels, D. Côté, and C. P. Lin, "Multiphoton Microscopy of Live Tissues With Ultraviolet Autofluorescence," *IEEE J. Sel. Top. Quantum Electron.* **16**(3), 516–523 (2010).
31. J. R. Lakowicz, H. Szmajski, K. Nowaczyk, and M. L. Johnson, "Fluorescence lifetime imaging of free and protein-bound NADH," *Proc. Natl. Acad. Sci. U.S.A.* **89**(4), 1271–1275 (1992).
32. T. Hato, S. Winfree, R. Day, R. M. Sandoval, B. A. Molitoris, M. C. Yoder, R. C. Wiggins, Y. Zheng, K. W. Dunn, and P. C. Dagher, "Two-Photon Intravital Fluorescence Lifetime Imaging of the Kidney Reveals Cell-Type Specific Metabolic Signatures," *J. Am. Soc. Nephrol.* **28**(8), 2420–2430 (2017).
33. A. F. Tarantal, H. Chen, T. T. Shi, C. H. Lu, A. B. Fang, S. Buckley, M. Kolb, J. Gauldie, D. Warburton, and W. Shi, "Overexpression of transforming growth factor-beta1 in fetal monkey lung results in prenatal pulmonary fibrosis," *Eur. Respir. J.* **36**(4), 907–914 (2010).
34. I. Pavlova, K. R. Hume, S. A. Yazinski, J. Flanders, T. L. Southard, R. S. Weiss, and W. W. Webb, "Multiphoton microscopy and microspectroscopy for diagnostics of inflammatory and neoplastic lung," *J. Biomed. Opt.* **17**(3), 036014 (2012).
35. H. Fehrenbach, "Alveolar epithelial type II cell: defender of the alveolus revisited," *Respir. Res.* **2**(1), 33–46 (2001).

## 1. Introduction

As optical imaging becomes crucial in the medical and life sciences, there has been a leap forward in biomedical imaging techniques over the past decade. Among many biomedical imaging techniques fluorescence lifetime imaging microscopy (FLIM) is especially powerful attributed by the merit of capturing the biochemical properties within various biological targets including cells and tissues, because the physiological processes that take place in these biological objects are mostly accomplished by the biochemical reactions [1, 2]. FLIM can visualize useful biochemical information such as ion density (ex. calcium, oxygen and hydrogen ion), protein-protein interaction (ex. fluorescence resonance energy transfer), and metabolic state (ex. nicotinamide adenine dinucleotide (NADH)) based on the principle that fluorescence lifetime varies depending on the local chemical density or composition [2–8].

Biochemical effectors such as signaling molecules or proteins are known to have their primary function as computational elements and to build various compartmentalized biochemical circuits within living cells and tissues [9]. Therefore, the information about the biochemical interactions should be obtained as a function of space and time to fully understand the structural state of cells and their underlying processes [8, 9]. More importantly, given the highly dynamic nature of the physiological processes of cells, high-speed imaging is essential to build a useful system to capture these phenomenological events. So far, the major obstacle utilizing FLIM in real-time imaging was the extensively long data acquisition and processing time.

Conventionally, time-correlated single-photon counting (TCSPC) have been used to obtain the lifetime of the fluorescence signal. Compared to the wide-field FLIM techniques utilizing time-gated intensifier combined with charge coupled devices (iCCD) [10, 11], TCSPC is beneficial for its higher compatibility with beam-scanning microscopy such as confocal microscopy or two-photon microscopy. Also, it is known to provide the highest precision among various types of lifetime imaging techniques. However, TCSPC directly counts single photons sequentially, therefore it requires a long acquisition time. The collected photon signals need additional reconstruction process to obtain the fluorescence decay curve, which will delay the data acquisition process even more. To overcome the low photon rate, TCSPC unit can be constructed in the multichannel array but it will become inevitably expensive [12]. Some FLIM systems utilize single photon avalanche diode (SPAD) array—that basically function as TCSPC array-coupled with multifocal beams to enhance the photon collection rate (number of collected photons per second), however obtaining high pixel rates with arrays of APDs is extremely expensive. Also, another major hurdle in establishing a real-time FLIM system using TCSPC method is its heavy computational process led by the iterative re-convolution process which extracts the lifetime value from the reconstructed fluorescence decay curve [13].

Latest high-speed digitizers enabled rapid data acquisition by directly sampling the fluorescence decay curve [6, 14–17]. Cheng et al. and Malik et al. introduced a real-time FLIM visualization of oral cancer *in vivo* utilizing hand-held FLIM device achieved 30-kHz pixel rate by using a digitizer with a sample rate of 6.25 GS/s [14, 15]. Dow et al. have developed a real-time FLIM system by synchronously interleaving the digitization process. Although the main digitization card was relatively slow (500 MHz), an oscilloscope with high sample rate (5 GS/s) independently measured IRF to compensate the limited bandwidth of detection devices [16]. Giacomelli et al. also suggested a rapid two-photon FLIM technique using direct temporal sampling (DTS) to acquire fluorescence lifetime images from the excised breast tissue [17]. Through direct fast sampling (1.76 GHz), their system achieved net pixel rate of 7.3 Mpps (pixels per second), but the lifetime visualization was done by post-processing after streaming the data into a solid-state drives array. The simplified deconvolution strategies have also been introduced to enable real-time visualization [15, 16], but this simplified deconvolution can compromise the accuracy of lifetime. Also, given that the fast digitization of direct sampling-FLIM limits the temporal window of the sampling

points, there is a possibility that the signal collection efficiency is low compared to the TCSPC. (Here, the signal collection efficiency can be regarded as the total number of sampling points for the signal or decay curve of each pixel.) Therefore, when detecting a decay curve with short lifetime or an instrument response function (IRF), the signal-to-noise ratio (SNR) of real-time imaging may decrease.

The analog mean-delay (AMD) method introduced by Moon et al. has suggested simplified way of deconvolution while maintaining the signal collection efficiency at a level similar to the conventional TCSPC methods [18]. During the data acquisition, this method stretches a pulsed fluorescence decay curve in the time domain using a low-bandwidth amplifier so that the digitizer with limited bandwidth can estimate the average arrival time of photons (the mean-delay value) taken from the departure time of each pulses at the pulse laser. Without assessing the exact lifetime curve, the lifetime value can be obtained by subtracting the average arrival time of the reflected signal, which can be considered as IRF, from that of the fluorescence signal. Moreover, the AMD method provides better signal collection efficiency at the limited sampling speed of the digitizer because it stretches the fluorescence pulse in time domain, and consequently maintains high SNR. In this sense, analog mean-delay (AMD) method is clearly an innovative approach that can realize the real-time fluorescence lifetime visualization by maximizing the photon rate of FLIM signal detection, and simplifying the computation process during the data analysis. There have been several reports applying the AMD method for implementing high-speed FLIM [18–25]. Our group also have reported an AMD-FLIM coupled with a single-photon near-infrared fluorescence (NIRF) microscopy and successfully measured and displayed the lifetime information from the 40-MHz pulsed laser in real-time utilizing line-triggering method and the high-speed parallel computing technique [23, 24]. Despite the fast detection speed of AMD method, previously developed AMD-FLIM systems still have some limitations for tissue tomography largely due to the low depth penetration and high photo-damage. In addition, the selection of fluorophores and the efficiency at visible excitation are limited since a near-infrared pico-second pulsed laser with a fixed wavelength (780 nm) has been utilized as a light source.

In this study, we developed a real-time two-photon fluorescence lifetime imaging microscopy (TP-FLIM) with a pixel rate of 3.91 MHz employing a wavelength-tunable femtosecond pulsed laser. The line-triggering method that has been developed in our previous work was employed for fast imaging especially because it enables the use of high frequency laser [24]. However, the line-triggering method needed to be additionally adjusted to our system that accommodates a femtosecond pulsed laser. On the notion that two-photon microscopy (TPM) can provide longer penetration depth in comparison to single photon excitation that was utilized at our previous NIRF-FLIM, we considerably improved the optical sectioning efficiency in thick biological specimen with lower photo-damage. Also, to augment the retrievable auto-fluorescence signals induced by the two-photon effect without any staining agent, we utilized a wavelength-tunable femtosecond pulsed laser which can be optimized for certain endogenous fluorophores. Consequently, we rapidly obtained auto-fluorescence signals and their lifetimes within the tissues, which are conceivably originated from the endogenous fluorophores such as nicotinamide adenine dinucleotide (NADH), flavin adenine dinucleotide (FAD), or elastin [26].

## 2. Materials and methods

### 2.1 The analog mean-delay (AMD) method

The detailed working principle of the AMD method can be found in previous works [18–20]. According to the exponential characteristic of the fluorescence decay curve, the fluorescence lifetime,  $\tau$ , can be expressed as follows:

$$\tau = \tau_{fl} - \tau_{irf} = \frac{\int t \cdot i_{fl}(t) dt}{\int i_{fl}(t) dt} - \frac{\int t \cdot i_{irf}(t) dt}{\int i_{irf}(t) dt} \quad (1)$$

where,  $\tau_{fl}$  and  $\tau_{irf}$  represent the mean-delays (or the first-order moments) of the fluorescence emission signal detected by the photodetector and the instrument response function (IRF,  $i_{irf}(t)$ ), respectively. Detected fluorescence emission signal is the convolution of temporal distribution of laser pulse, fluorescence decay function, and detector time-spread function. The IRF needs to be measured to extract the native fluorescence decay function ( $Ae^{-t/\tau}$ ) by deconvoluting the effect of the laser and the detector [18]. FLIM techniques conventionally utilize high-speed detection devices that can measure the fluorescence decay function and IRF as precise as possible to yield accurate lifetime through curve fitting. Unlike the conventional TCSPC-FLIM techniques, the AMD method just needs to measure the mean temporal delays ( $\tau_{fl}$  and  $\tau_{irf}$ ) through simple numerical integration of the sampled data that can be acquired by the detection devices with normal or even lower speed. To detect sufficient number of sampling points on the fluorescence decay curve and the IRF using low-speed detection devices, the AMD method is designed to intentionally stretch the signal, or the decay curve, using low bandwidth electronics. The limited bandwidth of the amplifier will affect both  $\tau_{fl}$  and  $\tau_{irf}$  (the mean-delay values), thus the effect will be cancelled out when  $\tau_{irf}$  is subtracted from  $\tau_{fl}$  as shown in Eq. (1). As this simple subtraction process is indeed a subtractive deconvolution process of IRF, the AMD method doesn't require recursive curve fitting of the fluorescence decay curve or complicated IRF deconvolution in frequency domain. Also, this process is simple enough to be done in real time and does not require post processing. Taken together, the AMD method is greatly useful for real-time imaging for its reduced computational burden and economically beneficial because it enables utilizing the low speed detection optics and electronics to measure the fluorescence lifetime precisely.

## 2.2 Optical imaging system

Figure 1 shows the schematic diagram of our high-speed TP-FLIM system. A wavelength-tunable femtosecond pulsed laser (Mira 900-F, Coherent) was used to generate two-photon excitation effect. A Faraday isolator (BB-05-I-800-000-900, Electro-Optic Technology) was used to block the backward light reflected by any succeeding optical components, then a set of two Glan-Taylor polarizers (GT5-B, Thorlabs) was installed to control the power of the femtosecond light. The range of power reaching onto the tissue (or at the focus of the objective lens) has been measured as  $< 1.3 \text{ J/cm}^2$ . The overall power range that we have used is below the maximum permissible exposure (MPE) which is shown to be  $1.38 \sim 1.74 \text{ J/cm}^2$  at  $750 \sim 800 \text{ nm}$  based on the American National Standard for the Safe Use of Lasers (ANSI Z136.1-2000) [27]. A negative chirping unit composed of a set of customized chirping prisms, a flat mirror, and a half-moon mirror were used to pre-compensate the group delay dispersion (GDD) caused by the following refractive optics, including a beam expander, a relay optic composed of three achromatic doublet lenses (one for tube lens and two for scan lens), and an objective lens, which can harm the two-photon efficiency significantly.

The scanning optics system was built with a scan lens, a tube lens, and a set of scan mirrors (6230H and CRS 4K, Cambridge Technology), that can scan two-dimensional field-of-view (varies from  $150 \text{ by } 150\text{-}\mu\text{m}$  to  $600 \text{ by } 600\text{-}\mu\text{m}$  imaged with  $1024 \text{ by } 1024$  pixels) with a frame rate of about 3.7 frames per second (fps). The scanning light was designed to enter into the back-infinity port of the fluorescence microscope (DMi8, Leica Microsystems), and focus on the specimen through a high numerical aperture (NA) objective lens (XLUMPLFLN-20XW, 1.0NA, Olympus). A motorized three-axis scanning module of DMi8 was used to navigate the specimen for the target region-of-interest (ROI), and to acquire three-dimensional images through the axial scanning.



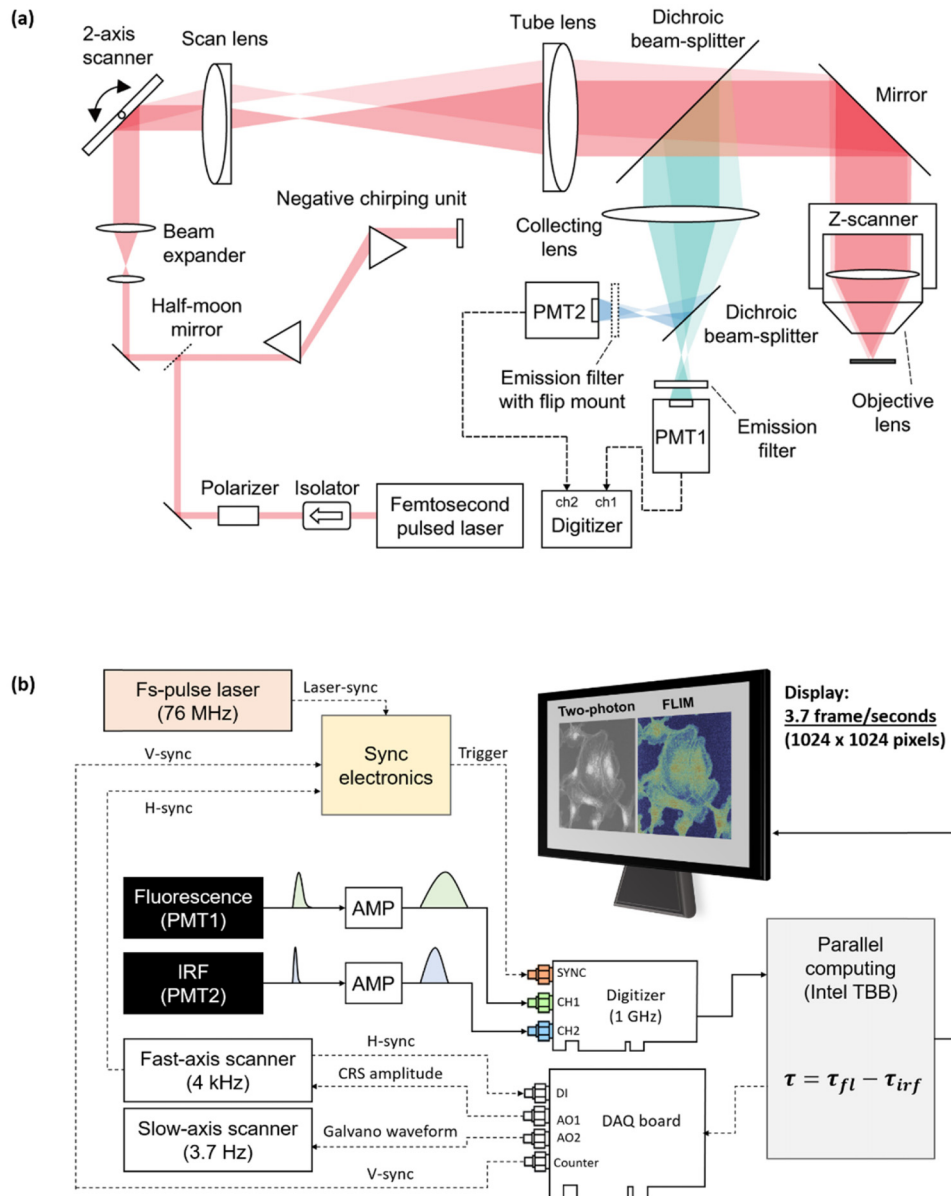


Fig. 1. (a) System schematic and (b) process flow diagram of high-speed two-photon fluorescence lifetime imaging microscope (TP-FLIM) (AO: Analog output, DI: Digital input).

The light signal from the specimen was reflected by a broadband mirror (21004, Chroma Technology) which was mounted on a filter cube installed at the DMI8 turret, then the two-photon emission signal was directed into the detection optics by a cold mirror (FF705-Di01, Semrock). This signal is mainly composed of two-photon fluorescence emission, however, it still contains the certain portion of back scattered light which is reflected at the cold mirror. The two-photon fluorescence emission was divided from the back-scattered light using a long-pass dichroic beam-splitter (Di02-R405, Semrock) and an emission filter (FF694/SP, Semrock), and detected by a highly sensitive photomultiplier tube (PMT1, H7422A-50, Hamamatsu Photonics). The back-scattered light was detected by another photomultiplier tube (PMT2, H7422P-40, Hamamatsu Photonics) and used as an instrument response function

(IRF) to calculate the fluorescence lifetime. Second harmonic generation (SHG) can be generated depending on the specimen during two-photon excitation if the specimen has non-centrosymmetric structure. The SHG signal could also be detected by placing an emission filter (FF424/SP, Semrock) in front of the PMT2 by using a motorized flip mount (MFF101/M, Thorlabs). In case that the specimen shows sufficient SHG emission across the ROI, SHG signal can be directly utilized as IRF. A collecting optics, composed of three singlet plano-convex lenses with anti-reflection (AR) coating in visible wavelength range, was carefully designed by using Zemax software to collect the light signals emitted through the DMi8 efficiently. The light signals detected by the PMTs were amplified by current-to-voltage amplifiers (C9663, Hamamatsu Photonics), and directly digitized using a high-speed 2-channel digitizer (U5309A, Keysight Technologies).

### 2.3 Data acquisition and processing

As shown in the process flow diagram (Fig. 1(b)), the fluorescence and reflection signal of each pixel are generated by the femtosecond pulsed laser, detected by PMTs, and stretched by low-bandwidth amplifiers. A built-in photodiode inside the femtosecond laser generates the laser-sync. A DAQ board (PCI-6733, National Instruments, USA) controls the fast-axis scanner, and, at the same time, receives the line-sync (H-sync) signal from the fast-axis scanner, then it generates frame-sync (V-sync) and waveform-signal for slow-axis signal scanner. In case of high repetition rate lasers, a digitizer cannot be triggered for every laser pulse because the trigger rearm speed of the commercial digitizer is limited. Therefore, we adopted a line-triggering method that we have developed in our previous work to fully utilize the fast laser repetition speed and enhance the imaging speed [24]. In our line-triggering method, the first laser pulse in each line composing an image frame is used for triggering the digitizer sampling. A custom-built sync electronics is used to generate the line-trigger signals by complexing laser-sync, H-sync, and V-sync. The pulse signals obtained by fluorescence and reflection channel are sampled by the digitizer, transferred to the main memory (RAM) in the computer, and then processed through repetitive numerical integration by our imaging software written in C++ and parallel computing library (TBB, Threading building block,

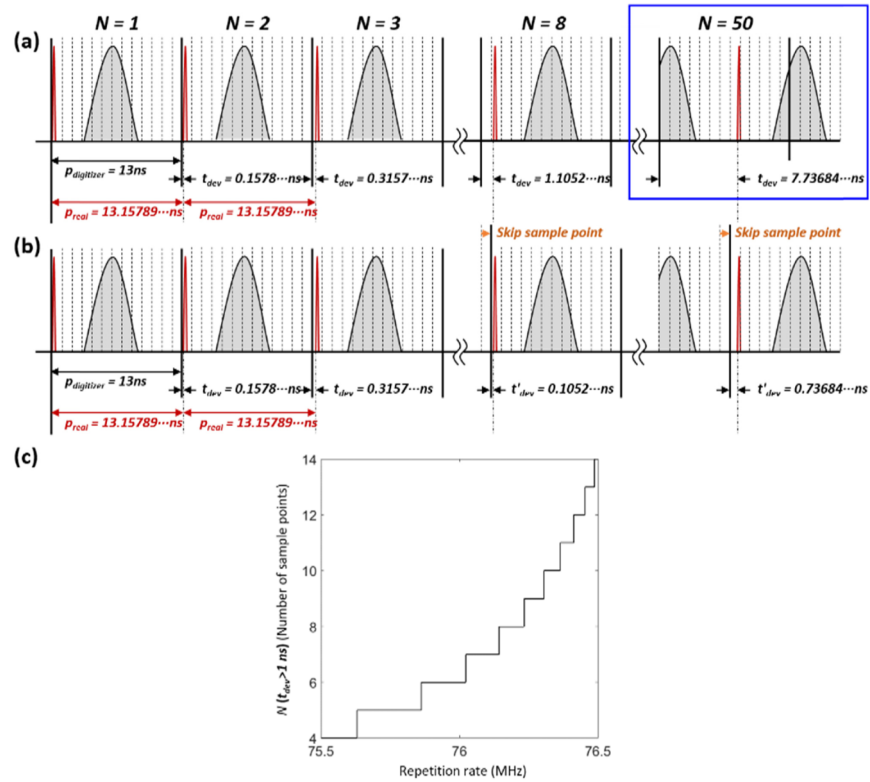


Fig. 2. An example of timing deviation between the laser sync (red curve) and the sample point of the digitizer (dotted black vertical line) in case the pulse repetition rate is 76 MHz, signal (gray curve): (a) initial state, (b) after applying the sample skipping algorithm, and (c) the relationship between the pulse repetition rate and the number of sample points ( $N$ ), every  $N^{\text{th}}$  sample point  $t_{dev}$  becomes larger than 1 ns.

Intel). At last, only the 8-bit intensity and lifetime values of each pixel is recorded to the hard disk drive (HDD) and the raw sampled data from the digitizer is discarded after processing [24]. The total time required for acquiring, processing, and visualizing TPM and FLIM images (1024 x 1024 pixels) is less than 0.27 seconds, and, within the time, the images are displayed on the screen in real-time.

#### 2.4 Measurement error and numerical compensation

Line triggering method is essential for fast imaging, but, if there exists a subtle timing deviation between the laser sync ( $t_{laser \ sync}$ ) and the sample point ( $t_{sampling}$ ), the error can be accumulated by every sample point along the scanned horizontal line and accordingly cause an error in the lifetime value. When the timing deviation ( $t_{dev}$ ) between the laser sync and the sample point is small, the error can be simply compensated numerically. However, the compensation process can become very complicated with the wavelength-tunable femtosecond laser that we used in this study, because the timing deviation ( $t_{dev}$ ) is relatively large and the compensation value should be adjusted according to the nominal pulse repetition rate which can vary depending on the longitudinal mode created in the laser cavity.

To understand the error occurrence caused by the timing deviation ( $t_{dev}$ ), we depict the periodic sample points of the digitizer (dotted vertical black lines), the laser sync signal (red), and the emission signal (gray) with respect to time along x-axis for 76 MHz pulse repetition rate (Fig. 2(a)). Each sample point is exactly 1 ns apart from the adjacent ones for 1-GHz digitizer. As the time interval between each sync signal (or laser pulse) is 13.15789... ns



marked as  $p_{real}$  in Fig. 2, the lifetime will be calculated from every 13 sample points and consequently the digitizing period ( $p_{digitizer}$ ) and a single measurement window is 13 ns long. As mentioned above, the interval between each sync signal ( $p_{real}$ ) is not an exact integer multiple of 13 ns, it is inevitable to have the timing deviation ( $t_{dev} = |p_{real} - p_{digitizer}|$ ) between the starting point of the sync signal and the digitizer sample point. During the line scanning the  $t_{dev}$  accumulates for every 13 ns and eventually the emission signal goes out of the measurement window as shown in the blue box of Fig. 2(a). To prevent the extreme accumulation of errors caused by  $t_{dev}$  and to keep the signal within the measurement window, the signal detection algorithm is designed to skip sample points of the data flow whenever  $t_{dev}$  becomes larger than 1 ns (Fig. 2(b)). This sample point skipping algorithm have been implemented in the data acquisition software that we have written in C++. The error described in Fig. 2(a) and 2(b) apply only to the case for the pulse repetition rate ( $f_{rep}$ ) of 76 MHz, but  $f_{rep}$  of a mode-locked laser can be changed depending on the cavity length. Thereupon, the algorithm was additionally fine-tuned for other possible  $f_{rep}$  and the corresponding timing deviation ( $t_{dev}$ ). As shown in Fig. 2(c), we have built a library file to support the sample point skipping algorithm; the algorithm ignores every  $N^{th}$  sample point at each corresponding  $f_{rep}$ . Through this way, the effective timing deviation ( $t'_{dev}$ ) value can be kept within 1 ns (Fig. 2(b)).

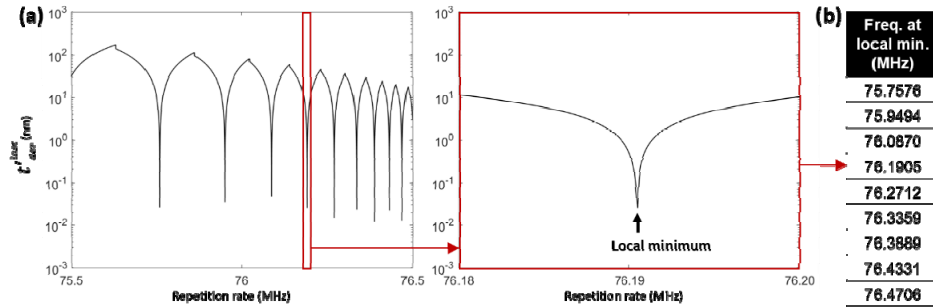


Fig. 3. (a) The pulse repetition rate (PRR) and its corresponding  $t'_{dev}^{last}$  value: for an example a PRR range that gives local minimum value is enlarge at the right side of the graph (red box), (b) a look-up table of the available PRRs.

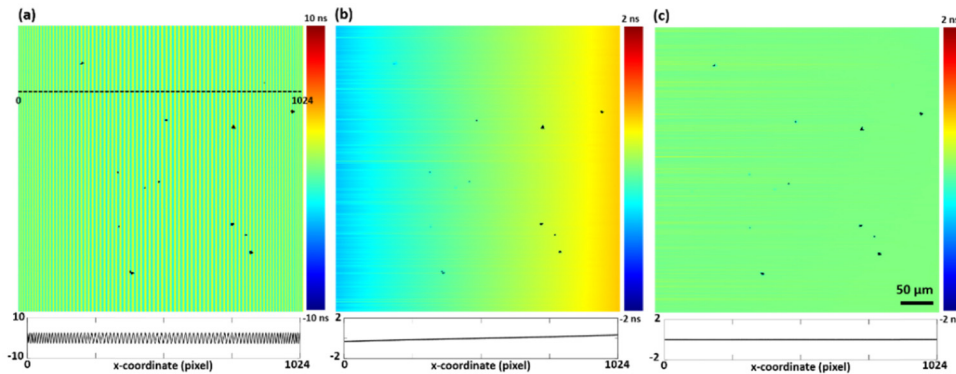


Fig. 4. FLIM image obtained by the reflected signal from a mirror surface for calibration and the bottom graph represents the lifetime value along the dotted line marked within the image: (a) initial image before any error correction, (b) image after skipping sample points when  $t_{dev}$  becomes larger than 1 ns, and (c) final image after numerical error correction.

Then, the next step is correcting the residual error reflected in the measured lifetime numerically, however the numerical correction is applicable only when  $t'_{dev}$  is small enough (less than 3 ns). Given that the error accumulates along the scanned horizontal line,  $t'_{dev}$  at the

last measurement window of each horizontal line ( $t'_{dev}{}^{last}$ ) has the largest value and we selectively used  $f_{rep}$  that gives the local minimum value of  $t'_{dev}{}^{last}$  (Fig. 3(a) and 3(b)). As mentioned earlier, the optical path length can alter  $f_{rep}$  of the cavity mode-locked laser, thus we finely regulated the path length of the laser light by modulating the position of the pre-chirp prism inside the laser cavity to obtain desired  $f_{rep}$  provided at the look up table in Fig. 3(b). In fact, the cavity mode-locked laser (Mira 900-F, Coherent) that we utilized in this study requires manual fine-tuning of the optical alignment inside the laser cavity almost every time it is turned on, anyway. Therefore, adjusting  $f_{rep}$  to the target value does not require additional effort or any supplementary devices. Since the signal reflected by a mirror is supposed to have 0 ns decay time (lifetime), we then used a mirror to numerically correct the residual error of our FLIM system. When we imaged a mirror, initially, the error generated by the timing deviation ( $t_{dev}$ ) periodically increases and decreases along the horizontal line as shown in Fig. 4(a). After applying the sample point skipping algorithm, images that have monotonically increasing lifetime along the horizontal direction were obtained (Fig. 4(b)). The error measured in Fig. 4(b) was then used as a reference and curve-fit along the x-coordinates to estimate the trend. The obtained error function was imbedded into our data acquisition software for numerical correction. At last, the numerical correction process generated an image that uniformly has 0 ns (Fig. 4(c)). To check the accuracy of the system, we then measured the lifetime of Coumarin 6 (Sigma-aldrich) dissolved in dimethyl sulfoxide (DMSO) and  $10^{-3}$  M Rhodamine B (Sigma-aldrich) dissolved in distilled water. The lifetime was measured to be  $0.24 \pm 0.01$  ns and  $1.41 \pm 0.01$  ns, which is close to the ones known as (0.31 ns) and ( $1.49 \pm 0.04$  ns), respectively [28, 29].

## 2.5 Imaging samples

To test our TP-FLIM system on cells, FluoCells Prepared Slide #1 (F36924, Thermo Fisher Science) was used. Prepared Slide #1 consists bovine pulmonary artery endothelial cells (BPAECs) that are stained with three different labelling agents on different subcellular parts; MitoTracker Red CMXRos (ex/em 579/599 nm) on mitochondria, Alexa Fluor 488 Phalloidin (ex/em 495/518 nm) on actin fibers (F-actin), and DAPI (ex/em 358/461 nm). Also, to test the possibility of two-photon tissue tomography, we prepared kidney and lung tissue excised from a 5-weeks old healthy CD-1 mouse. Only the endogenous fluorophores of the fresh tissues were imaged by our TP-FLIM system without using any labeling agent.

### 3. Experimental results

#### 3.1 2D imaging performance test using cell

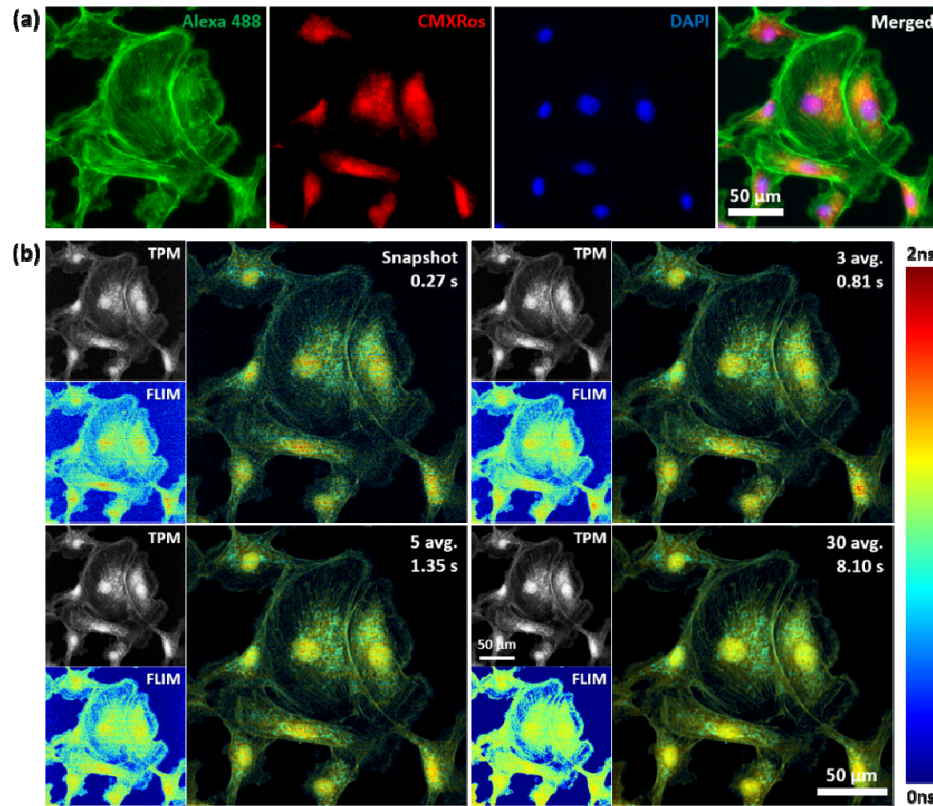


Fig. 5. (a) Wide-field fluorescence images and (b) TP-FLIM images of stained BPAEC. The number of averaging and the imaging time are written within each image.

Given that the fast data acquisition speed of the AMD method is primarily attributed to maximizing the photon collection rate, it can raise concerns about whether the lifetime measurement performance will be deteriorated under the photon-limited conditions including high speed scanning. High speed scanning will shorten the pixel dwell time, consequently the photon collection rate can be dramatically reduced. In this context, we examined the lifetime measurement performance at the highest possible measurement speed (3.7 fps) of our system using cell sample. First, we captured the structural trait of nucleus, F-actin, and mitochondria with a wide field fluorescence microscope using the mercury metal halide bulb as light source and dichroic filters (DMi8, Leica) for our reference (Fig. 5(a)). F-actin is a fibrous structure and can be seen around the cellular boundary and across the cytosolic area of cells. Mitochondria looks like small dots or short strings that are mostly located around cell nucleus. Then, we have obtained TP-FLIM image (Fig. 5(b)). The lifetime signal exhibited around F-actin labelled with Alexa Fluor 488, mitochondria labelled with Red CMXRos, and nucleus labelled with DAPI were shown to be slightly different from each other ( $\sim 0.9$  ns,  $\sim 0.7$  ns, and  $\sim 1.1$  ns, respectively) as different type of fluorophores will have different values of lifetime. More importantly, even in snap shot image with short pixel dwell time (85 ns), the measured fluorescence lifetime is shown to be almost identical as the one with longer dwell times (255 ns, 425 ns, and 2500 ns at 3-, 5, and 30 averaging, respectively), thus shows that the performance of our FLIM system is high enough to capture the lifetime at low photon

rate. Accordingly, thanks to the high photon efficiency of the AMD method, this data supports that our TP-FLIM system is qualified for the fast and further the real-time imaging.

### 3.2 Tissue Imaging

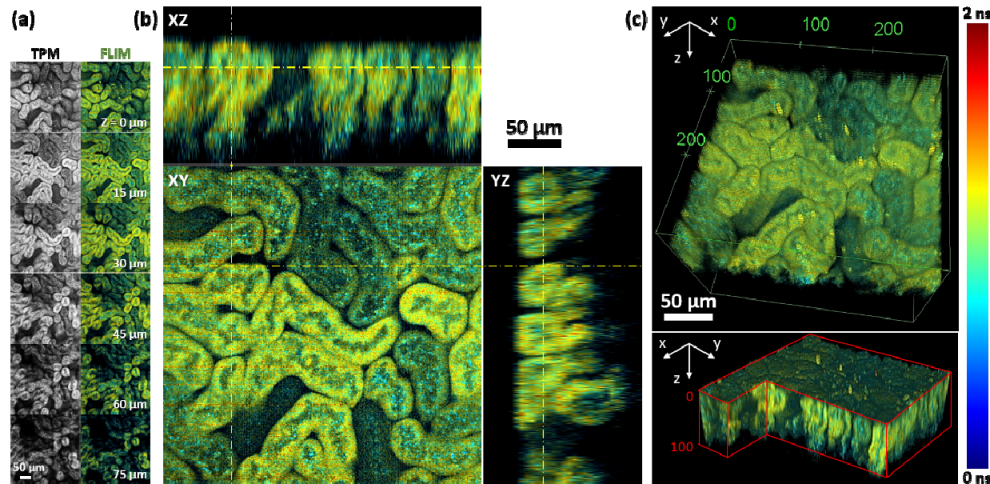


Fig. 6. Mouse kidney tissue: (a) cross-sectional images of TPM and FLIM along z-axis, (b) cross-sectional image at XY, XZ, and YZ plane, and (c) 3D rendering.

TP-FLIM images were acquired along the z-axis of the kidney tissues from a mouse. Even though 10 successive images were averaged for each 2D section, it took only 2 minutes to acquire the 3D volume with forty-five 2D sections. The total imaging depth was 225-μm and it was composed of a stack of images separated by 5-μm apart. The kidney tissues were not stained with any labelling agent, thus the auto-fluorescence signal was detected. According to the previous reports, the auto-fluorescence by two-photon excitation within the bandwidth of 400 – 600 nm contains the signal from the endogenous fluorophore NADH and FAD [30]. Indeed, the fluorescence lifetime of NADH become increasingly important in biomedical research because it reflects the chemical state of NADH and further the metabolic state of cells [31]. In the TPM images at Fig. 6, two-photon excitation demonstrate the distinct tubular structure of distal and proximal tubules in the renal cortex. FLIM signals exhibited spatial variation across the field-of-view and, especially, the tubular cells and the cells lining inside the tubular layer shows considerable contrast as 0.8 ns and 1.3 ns, respectively. The TPM intensity at the tubular lumen is very low, thus we could not achieve a meaningful lifetime signal within the luminal area. As the depth of penetration of the near-infrared laser light is substantially longer than visible light, TPM obtained the images in a depth of ~100 μm from the tissue surface without adjusting the laser output power along the axial depth of scanning (Fig. 6(a)-6(c)). Given that the experiment was not performed in vivo, the metabolic state shown in the FLIM image may not reflect the one of the live mouse, however we confirmed that the TP-FLIM image presents similar structural and biochemical hallmarks shown in previous studies [32].

Similarly, the lung tissue of a healthy mouse was also imaged with 760-nm excitation laser without staining process as shown in Fig. 7. To capture various architectures of the lung, both the cutting plane (Fig. 7(a)) and the surface area of the lung (Fig. 7(b) and 7(c)) have



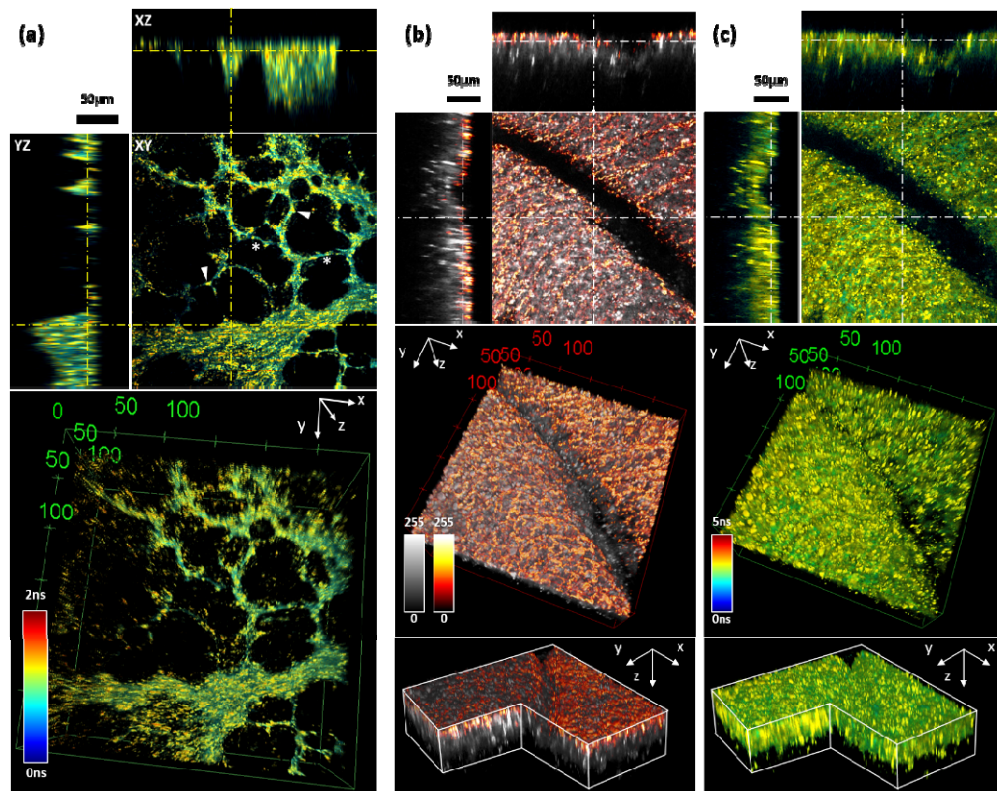


Fig. 7. The lung tissue images of 5-weeks old healthy mouse: (a) FLIM images taken at the cutting plane, (b) composite images of TPM and SHG, and (c) FLIM images taken at the surface area of the lung tissue.

been investigated. As shown in Fig. 7(a), the wall of alveolus expresses two different lifetimes; the areas expressing short lifetime ( $\sim 0.9$  ns, marked as white star in Fig. 7(a)) are relatively thin compared to the ones with long lifetime ( $\sim 1.3$  ns, marked as white arrow in Fig. 7(a)) that are thick and form protrusions into the alveoli lumen. Based on these morphological traits of the region expressing short and long lifetime, we assume that the tissues or cells composed of type I and type II pneumocytes, respectively [33–35]. Some of the protrusions with long lifetime seen at the alveoli wall may be the macrophages that are also known to be rounded and large, but they are not distinguishable from the type II pneumocytes at this point. To specify each part, additional comparative study with a histologic image that is individually labelled to type I, type II pneumocyte, and alveoli macrophage is needed.

As noted above, the IRF detector (PMT2) were also utilized as SHG detector. In Fig. 7, SHG and TP-FLIM signal are obtained from the surface area of the lung. SHG signal typically captures the collagen bundles within the biological samples. It is natural to have minimal or no collagen deposition sites within the alveoli tissues, unless the lung has a sign of any pathological condition such as fibrosis [33, 34]. Not surprisingly, as our mouse was a healthy subject, we did not capture a strong SHG signal from the alveolus wall (Fig. 7(a)). However, the thicker tissues such as the tissues of the lung surfaces or around the bronchioles contains appreciable amount of collagen and we detected a thin layer of collagen at the outermost layer of the lung as shown in Fig. 7(b) and 7(c) [33]. The lung tissues are mainly composed of type I and II pneumocytes, thus we speculate most of the TPM auto-fluorescence signals can be originated from them [35]. Also, the signal may include the one from the thin elastin layer deposited at the lung surface. In the middle of the tissue, there is a



notable valley-like structure which seems to be the joint area between two groups of alveoli bundles. However, to evaluate each part of the tissues more precisely and to confirm the source of the different lifetime, additional histological study need to be done.

Last but not least, we provide a video that captured the moment of lung tissue imaging to demonstrate that our microscope system visualizes robust lifetime value in real time ([Visualization 1](#), the range of the lifetime color-bar in the video is 0 to 5 ns). As can be seen from the [Visualization 1](#), we can simultaneously observe the structural and chemical properties (lifetime) of the tissues at the display window while searching for the region of interest.

#### 4. Discussion

The key requirements for live tissue imaging can be specified as follows; 1. long penetration depth, 2. low photo-damage, 3. high imaging speed, and 4. real-time visualization. It is relatively easy to meet the first three conditions using conventional TCSPC-based FLIM systems including the techniques utilizing array detectors, but the last one-real time visualization-is almost impossible attribute to the long data reconstruction and deconvolution process of TCSPC method. Therefore, instead of TCSPC, we integrated AMD method in our TPM system and successfully accomplished real time visualization of FLIM images taken from deep tissues for the first time. Our TP-FLIM system simultaneously images and visualizes FLIM images at a rate of 3.7 frame per second (fps) (or 3.91 mega pixels per second), which is indeed below the speed conventionally categorized as “video-rate”. However, considering that the average processing time required for calculating a lifetime value of each pixel (~68 ns) are currently measured to be shorter than the average pixel dwell time of the 8-kHz resonant scanner (~80 ns), the frame rate of our system can be easily improved up to 30 fps without changing the actual pixel dwell time by using 8-kHz bi-directional scanning technique and reducing the image size to 512 x 512 pixels.

A high repetition rate laser is advantageous to establish a fast imaging system, whereas it also derives some technical difficulties. One can occur by the significant discrepancy between the trigger rearm speed of the digitizer and the laser sync speed, and we have solved this problem by utilizing a line-triggering method and additional numerical compensation as described above. For an alternative approach, this problem can be solved by synchronizing the clock of the digitizer directly to the laser sync signal by adding a phase locked loop (PLL) circuit as other researchers have introduced [16, 17]. We did not adopt this method for this time by the reason that it required additional electric circuit. Another technical complication can be caused by the short intervals between laser pulses. Sometimes the intervals between pulses are too short to measure the full fluorescence decay curve without any interference of the following fluorescence signal occurred by the succeeding pulse. The maximum fluorescence lifetime that can be measured within 1% accuracy using a pulsed laser is generally known to be about one-eighth of the pulse period. As AMD-FLIM method intentionally stretches the fluorescence signal in the time domain, the measurable lifetime range will be even shorter than this [18]. As a result, the measured lifetime value of our system can be lower than its actual value considering the short pulse period (~13 ns) of 76-MHz high frequency laser. Nevertheless, the precision of the system is sufficiently high so the lifetime contrast can be imaged and used for the investigation of the tissue. Given the background, in this study, we focused on measuring the spatial distribution and the relative difference of the fluorescence lifetime rather than specifying the exact values of the lifetime. In the future, we are planning to incorporate devices such as pulse picker, or cavity dumper into our pulsed laser, which can modulate the pulse repetition rate and increase the pulse period (ex. 130-ns with the division ratio of  $f_{rep}/10$ ) to improve the lifetime measurement accuracy.

The last issue that we can be discussed is the non-specificity of the emission signal that have obtained. We utilized a broadband short pass emission filter with the cut-off frequency

of 700-nm for the two-photon signal acquisition emission filter. The emitted auto-fluorescence signal can be assumed to include the indicator of the metabolic activity (NADH) based on the excitation wavelength that we used, but we were not able to accurately specify the target fluorophore in this study due to the broad bandwidth of the emission filter. In future investigations, we are planning to specify the source of two-photon signal among various endogenous auto-fluorescence by utilizing an emission filter with a narrower bandwidth. Also, we can employ various exogenous fluorescence molecules to further target the specific biochemical reactions and enhance SNR.

### **Funding**

Research Foundation projects supported by Korean government (NRF-2014R1A6A3A04059713); Chungcheongbuk-do Value Creation Program.

### **Acknowledgments**

This study protocol was reviewed and approved by the Institutional Animal Care and Use Committee (IACUC) of National Cancer Center Research Institute (NCC-17-386). NCCRI is an Association for Assessment and Accreditation of Laboratory Animal Care International (AAALAC International) accredited facility and abide by the Institute of Laboratory Animal Resources (ILAR) guide.

### **Disclosures**

The authors declare that there are no conflicts of interest related to this article.